ChemistrySelect

Research Article
doi.org/10.1002/slct.202304373

Chemistry Europe
European Chemical Societies Publishing

www.chemistryselect.org

One-Step Synthesis of Metal Oxide Nanoparticles Using Cannabidiol: Characterisation and Cytotoxicity Assessment in Human Keratinocyte Cells

Andrea Jess Josiah,[a, b] Sreejarani Kesavan Pillai,[a] Werner Cordier,[c] Margo Nell,[c] Namrita Lall,[d, e, f] Danielle Twilley,[d] and Suprakas Sinha Ray*[a, b]

This research paper explores the field of nanobiotechnology, focusing on the design, characterisation, and potential dermal applications of metal oxide nanoparticles (MONPs). ZnO and FeO NPs exhibit distinctive properties that are valuable in dermato-cosmetic applications and transdermal drug delivery. This study investigates Cannabidiol (CBD) as a capping agent for MONPs synthesis. Employing microwave-assisted techniques, MONPs were synthesised using either CBD or polyvinylpyrrolidone (PVP) as capping agents. The TEM, SEM, FTIR, and XRD characterisation results confirmed the successful formation of CBD-capped ZnO and FeO NPs exhibiting an average particle size of 90 and 76 nm, respectively. The cytotoxicity of CBD-capped MONPs was evaluated on HaCaT cells over a concentration range of 100 to 6.25 μg/mL, which revealed that CBD-capped ZnO NPs exerted a cytotoxic effect on HaCaT cells (IC_{50} 85.34 ± 1.17 μg/mL). In contrast, CBD-capped FeO NPs and PVP-capped MONPs exhibited negligible cytotoxicity (IC_{50} > 100 μg/mL). TEM analysis revealed a noticeable structural alteration of ZnO NPs in the supplemented cell culture medium, which could contribute to enhanced NP uptake, thereby explaining the more pronounced cytotoxic effect of ZnO NPs. Therefore, the disparity in cytotoxic responses can be attributed to the protein coating adhering to the NPs surface in a biological medium.

Introduction

The integration of nanotechnology and biotechnology has resulted in the development of an advanced technical and scientific discipline referred to as nanobiotechnology.[1] A key element of this discipline involves the design, fabrication, and characterisation of materials and devices, where at least one exterior dimension ranges between 1 and 100 nanometers (nm).[2] Owing to their structural dimensions, nanomaterials are categorised into zero-dimensional (nano-onions, nanoparticles, quantum dots), one-dimensional (nanobelts, nanopillars, nanowires, nanotubes), two-dimensional (graphene), and three-dimensional (mesoporous carbon) materials.[3] Nanobiotechnology highlights the critical role of nanoscience and nanotools in developing innovative biomaterials for tissue engineering, nanopores for the expedition of single molecule transportation in DNA sequencing, nanosensors for diagnostics, medicinal devices, and theragnostic materials.[4] Nanomedicine is a predominant subfield of nanobiotechnology, and its primary function is the manipulation of engineered nanoparticles (NPs) for therapeutic and diagnostic applications.[5] When materials are synthesised at a nanoscale, their properties differ from their bulk counterparts. A fundamental feature of NPs is a larger surface area-to-volume ratio, which results in greater reactivity, catalytic activity, and other unique physical and chemical properties.[6] Moreover, it is possible to further tailor the properties of NPs to specific applications by controlling the size, shape, and surface chemistry during the synthesis process.

Due to their distinctive characteristics, MONPs are beneficial in multiple dermato-cosmetic applications.[7] Previous studies indicate that zinc oxide NPs (ZnO-NPs) displayed several

[a] A. J. Josiah, S. K. Pillai, S. S. Ray
Centre for Nanostructured and Advanced Materials,
Council for Scientific and Industrial Research,
Pretoria 0001, South Africa
E-mail: rsuprakas@csir.co.za
ssinharay@uj.ac.za

[b] A. J. Josiah, S. S. Ray
Department of Chemical Sciences,
University of Johannesburg,
Doornfontein 2028, Johannesburg, South Africa

[c] W. Cordier, M. Nell
Department of Pharmacology,
University of Pretoria,
Pretoria 0002, South Africa

[d] N. Lall, D. Twilley
Department of Plant and Soil Sciences,
University of Pretoria,
Pretoria 0002, South Africa

[e] N. Lall
School of Natural Resources,
University of Missouri
Columbia, MO 65211, USA

[f] N. Lall
College of Pharmacy,
JSS Academy of Higher Education and Research,
Mysuru 570015, India

biological activities such as antimicrobial,[8] antifungal,[9] anticancer,[10] and wound healing.[11] However, the leading quality of ZnO-NPs is incorporating them into sunscreens. Larger ZnO-NPs (200–400 nm) reflect and scatter light, resulting in a noticeable white tint on the skin; however, smaller particles (40–100 nm) can absorb visible wavelengths and subsequently disperse ultraviolet radiation, generating a transparent sunscreen.[12] Similarly, iron oxide NPs (FeO-NPs) show anticancer,[13] anti-inflammatory,[14] and antifungal[15] properties. These attributes play a beneficial role in the transdermal delivery of drugs.

Transdermal drug delivery (TDD) is a form of drug administration via the skin, enabling systemic circulation entry.[16] TDD has several advantages compared to traditional drug administration routes (oral or intravenous). Transdermal drug delivery allows for controlled drug release over an extended time, which aids in maintaining a consistent drug concentration in the circulatory system.[17] This can increase therapeutic effectiveness and reduce the risk of adverse effects related to drug concentration fluctuations. Transdermal delivery is non-invasive, resulting in a more patient-friendly approach to drug administration.[18] Additionally, TDD can improve drug bioavailability by circumventing the first-pass metabolism in the liver. This is particularly useful for drugs that may be degraded or metabolised by digestive enzymes or cause gastrointestinal irritation. Transdermal drug delivery decreases systemic side effects associated with traditional drug administration routes, as the drug is delivered directly to the site of action, and lower doses can be used to achieve therapeutic effects.[19] In a study by S. Kothawade *et al.*,[20] a transdermal patch loaded with ZnO-NPs was developed and evaluated for antimicrobial activity. The optimised patch demonstrated extended-release and improved bioavailability of ZnO-NPs, exhibiting antimicrobial effects against *Escherichia coli, Bacillus subtilis, Aspergillus niger*, and *Candida albicans* after 48 h exposure at 100 μg/mL. Another study by Abu-Huwaji *et al.*,[21] investigated the cytotoxic activity of ZnO-NPs loaded on transdermal patches against triple-negative breast cancer (TNBC) and human dermal fibroblast (HDF) cell lines. The ZnO-NPs, tested at concentrations ranging from 0.16 to 2.5 μg/mL for 24 hours, exhibited IC_{50} values of 0.42 μg/mL on TNBC and 1.5 μg/mL on HDF. The transdermal patches demonstrated sustained release of ZnO-NPs over 25 hours, with a steady-state flux of 7.21 μg/h/cm^2.

Raviraj *et al.*,[22] conducted an *in-vivo* analysis to explore the co-administration of FeO-NPs and 5-fluorouracil (5-FU) via transdermal delivery against melanoma cells. A combination of 5-FU (1 mM) and 10% FeO-NPs (1 mg/mL) with a dosage of 60 μL, was topically applied three times per week. The results demonstrated a substantial decrease in tumour growth following the topical administration of 5-FU with FeO-NPs, compared to the application of 5-FU alone. Afiune *et al.*,[23] synthesised FeO-NPs loaded with finasteride (FIN) or dutasteride (DUT) at 250 μg/mL and 125 μg/mL, respectively, for topical alopecia treatment. Cutaneous penetration studies were conducted for 12 or 24 hours. The loaded nanosystems demonstrated increased skin penetration compared to control solutions. DUT-loaded nanosystems exhibited higher retention in the stratum corneum than FIN-loaded nanosystems. After 24 hours, FIN-ION showed nearly double the amount of FIN in the skin compared to the control solution (18.64 ± 0.69 μg/cm^2 and 10.65 ± 0.38 μg/cm^2, respectively), while DUT-ION exhibited almost four times the amount of DUT (4.66 ± 0.45 μg/cm^2 and 1.24 ± 0.27 μg/cm^2, respectively).

The use of metal oxides in dermal applications has paved the way for innovative approaches to drug delivery and therapeutic interventions. These nanosystems have demonstrated the potential to enhance the penetration and retention of drugs in the skin.[24] To facilitate this, amphiphilic capping agents are employed in trace amounts during NPs synthesis.[25] These agents functionalise and stabilise NPs, while also preventing NPs agglomeration.[26] Chemical capping agents, including polymers (PVP, PEG, and PGA), present challenges in desorption kinetics from NP surfaces. The nonbiodegradable nature and potential cytotoxicity of these conventional capping agents highlight the demand for alternatives. Consequently, the pursuit of green capping agents has garnered considerable attention, with the dual objective of safeguarding biological systems and environmental integrity.[27]

Cannabidiol (CBD), a non-psychoactive compound derived from the *Cannabis sativa* plant, has gained attention for potential therapeutic applications in dermatology.[28] Employing CBD in MONP synthesis could improve bioavailability, facilitate targeted delivery to specific skin layers or cells, and optimise therapeutic outcomes. The molecular configuration of CBD comprises a terpenoid moiety, a phenolic hydroxyl group, and an alkyl side chain.[29] Phenolic compounds can exert non-covalent and covalent interactions in a diverse range of inorganic materials, including metals, semiconductors, carbon, silica, metal ions, and metal oxides. Furthermore, these compounds exhibit distinct physicochemical interactions, such as hydrogen bonding, metal coordination, covalent bonding, and interactions (electrostatic, π, and hydrophobic) between fundamental molecules of the inorganic material.[30] Natural phenols containing hydroxyl and carboxyl functional groups demonstrate protonation and absorption capabilities.[31,32] The mechanism governing the surface absorption of phenolic compounds onto metal NPs (MNPs) can be elucidated by the formation of an absorptive bond between the carboxyl group and the metal atom.[33] The MNPs synthesised via phenolic compounds exhibit enhanced stability when compared to their counterparts using conventional reducing agents, such as citrate or sodium borohydride.[34] Three specific configurations are used by phenolic functional groups to adhere to the surface of an MNP: monodentate ester-like bonding, bidentate bridging bonding, and bidentate chelating bonding.[33]

CBD interacts with the endocannabinoid system (ECS) as a partial agonist for CB1 and CB2 receptors. In addition, CBD inhibits the enzyme fatty acid amide hydrolase (FAAH), leading to increased anandamide levels and enhanced ECS activity. This modulation of the ECS contributes to CBD's anti-inflammatory and analgesic effects.[35] This finding is further supported by Petrosino *et al.*,[36] who demonstrated the anti-inflammatory properties of CBD; therefore, CBD could be considered a potential treatment for skin disorders characterised by inflam-

mation, such as acne, eczema, and psoriasis.[37] Studies have demonstrated the ability of CBD to attenuate oxidative stress in various dermal disorders, highlighting its potential as a topical antioxidant.[38,39] CBD demonstrates an antioxidant effect by scavenging detrimental free radicals, which mitigates oxidative damage to keratinocytes.[40]

Based on the above discussion, in this study, we investigated: Firstly, the synthesis of MONPs via CBD as a green functional capping agent. Secondly, a comparison of capping efficiency with the conventional synthetic capping agent PVP. Finally, evaluating the cytotoxic effect of both PVP and CBD-capped MONPs on HaCaT cells. The dual action of CBD as an antioxidant and anti-inflammatory agent makes it a promising candidate for dermal applications to address oxidative stress and inflammation-related skin issues.

Results and Discussion

Nanoparticle synthesis

Metal oxides ZnO and FeO-NPs were synthesised using: (i) PVP and (ii) CBD as capping agents. PVP is considered a stable, non-toxic,[41] non-ionic[42] multipurpose polymer that serves as a surface stabiliser, growth modifier, and NP dispersant. A beneficial characteristic of PVP in NP synthesis is NP aggregation prevention, which is primarily due to the steric hindrance effect.[43] The PVP-capped NPs served as a reference to CBD-capped NPs. The phenolic compounds in CBD chelate Zn and Fe metal ions, forming stable complexes. This phenomenon is attributed to the phenolic compounds' capacity to donate electrons and hydrogen atoms. The stability of phenolic hydroxyl groups is attributed to the resonance of aromatic radical structures.[44]

The PVP-capped ZnO-NPs yielded a white precipitate upon the addition of sodium hydroxide (NaOH), which is consistent with previous literature;[45] however, upon the addition of CBD to the precursor salt ($Zn(NO_3)_2$), a mild precipitation reaction was observed evidenced by a colour change from colourless to a light white hue, which could be attributed to the formation of ZnO by the action of polyphenols present in CBD on zinc nitrate. The subsequent addition of NaOH to the reaction mixture resulted in a white precipitate, which indicated the formation of ZnO (the intermediate zinc hydroxide was converted to ZnO during calcination.[45]

A colour change accompanied by precipitation was observed during the synthesis of FeO-PVP NPs. A deep red precipitate was obtained when NaOH was added. Previous literature reported similar findings, with a description of fine red powder after synthesising FeO NPs[46]. The synthesis of FeO-CBD NPs yielded a similar synthesis reaction outcome when compared to ZnO-CBD NPs, where CBD was observed to function as a mild precipitating agent, evidenced by a colour change from colourless to an opaque red. The colour intensity and precipitation were enhanced upon the addition of NaOH. The sample obtained after synthesis can be described as a fine red powder and soft in texture, which is consistent with previous reports.[46]

Additionally, Oliveira *et al.*[47] explained that a precipitation reaction in metallic ion systems follows three sequential steps: from an amorphous hydroxide to a crystallised hydroxide and finally to an oxide[47].

Size and morphological analyses

The size and morphological features of the MONPs were captured by TEM. Figure 1(a) illustrates a distribution of polydispersed and heterogeneous ZnO-PVP NPs, with an average particle size of approximately 85 nm. These NPs exhibit diverse morphologies that include rectangular-shaped NPs, nanocubes, and spherical ZnO-PVP NPs. A study by Kamari *et al.*[48] synthesised PVP-capped ZnO NPs using a hydrothermal synthesis route to assess the efficiency of PVP as a capping agent. The research group observed particles to be elliptical or spherical, which partially correlates to the TEM images in the current study. Figure 1(b) displays the lattice fringes of a single ZnO crystal with a d-spacing of 0.258 nm corresponding to the interlayer spacing of the (002) plane.[49] Figure 1(c). The morphology of ZnO-CBD NPs can be described as non-uniform bulky elliptical disks and spheres. These NPs appear to exhibit polydispersity and have a large size range, with a particle size of $\pm$90 nm. Lattice fringes of ZnO are presented in Figure 1(d), where the inter-planar spacing is 0.2797 nm, which corresponds to the (100) plane of ZnO[50]

Figure 1(e) displays a TEM image of FeO-PVP NPs, that exhibits heterogeneous, polydispersed NPs, composed of square and flake-like structured particles. Silva *et al.*[51] investigated if the quantity of PVP influenced the size and crystalline nature of FeO nanostructured particles using the sol-gel method. The results showed NPs with a hexagonal morphology, with a particle size range of 25–45 nm. When comparing the TEM results in the current study to Silva *et al.*,[51] it is evident that employing PVP as a capping agent can produce various NP morphologies under different synthesis conditions. The lattice fringes of FeO-PVP NPs in Figure 1(f) have a d-space value of 0.266 nm, representing the Miller index of (110).[52] Figure 1(g) displays a TEM image of FeO-CBD NPs, which reveals diamond-like structured NPs that appear to have minimal agglomeration and an average particle size of ~76 nm. Additionally, an investigation of a single FeO crystal was carried out by HR-TEM analysis, depicted in Figure 1(h). Distinct lattice fringes can be observed, and a d-spacing value of 0.3606 nm was identified. The d-spacing value correlates to the (012) plane of structured FeO.[52]

SEM and EDS respectively determined the surface structure and elemental composition of both ZnO and FeO NPs. Figure 2(a) shows a clustered composition of ZnO-PVP NPs, which correlate to the TEM observations, and the EDS reveals a spectrum devoid of impurity peaks, where Zn has a weight percentage of 81.50%. Figure 2(b) shows a variety of elliptical disk-shaped ZnO-CBD NPs, along with smaller indistinct NPs observable in the SEM image, which correlates to the TEM

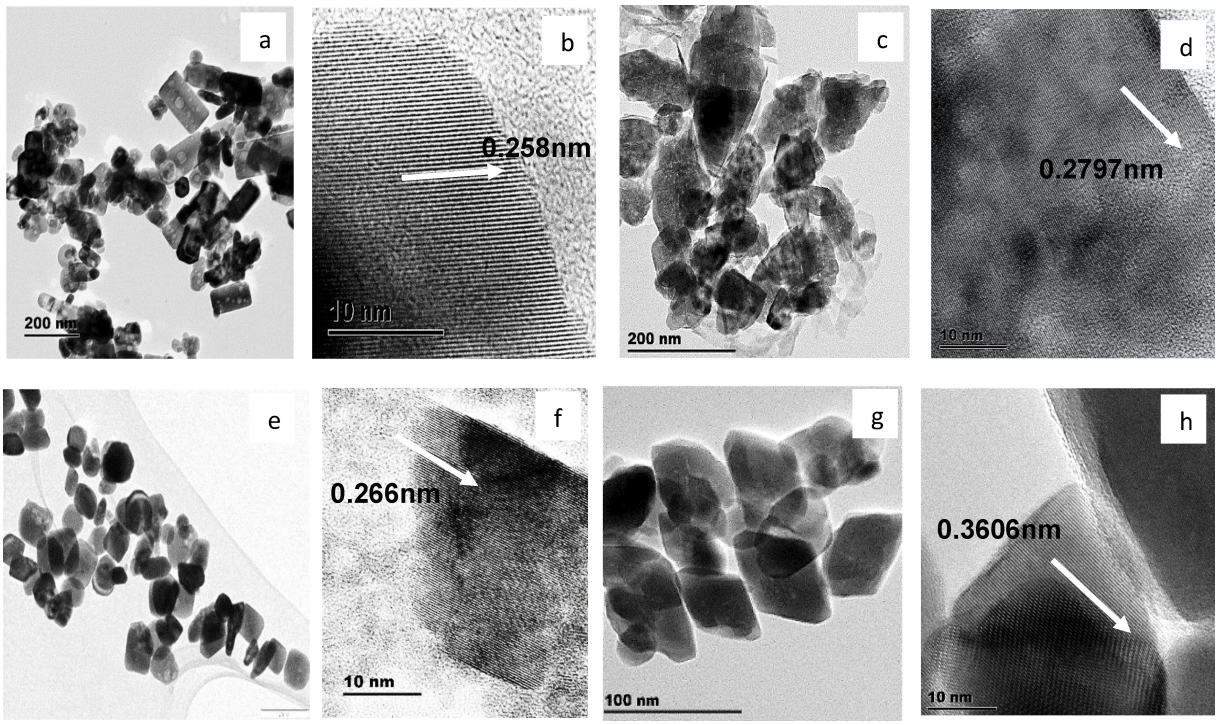

Figure 1. Morphology and size analyses of NPs; (a-b) PVP-capped ZnO NPs, (c-d) CBD-capped ZnO NPs, (e-f) PVP-capped FeO NPs, and (g-h) CBD-capped FeO NPs.

observations. The EDS spectrum shows no impurity peaks, indicating the high purity of ZnO NPs, with a total weight percentage of 87.05% for Zn. capped FeO, and (d) CBD-capped FeO.

Figure 2(c) shows square-like NPs for PVP-capped FeO NPs, which correlates to the TEM data, however, the individual NPs assembled in clusters. The EDS spectrum of FeO-PVP NPs reveals a high purity of Fe with a weight percentage of 72.74%. Figure 2(d) reveals polydispersed, diamond-like NPs, correlating to the TEM observations. The EDS spectrum illustrates the Fe and O peaks with a total weight percentage of 78.57%, indicating an above-average purity in the synthesised sample.

The crystallinity and structural composition of metal oxide NPs were analysed by XRD. Figure 3(a) presents the diffraction pattern of ZnO-PVP, which exhibit peaks at $2\Theta = 31°$, 34°, 36°, 47°, 56°, 62°, 66°, 68°, 69°, 72° and 77° which correspond to the indices; (100), (002), (101), (102), (110), (103), (200), (112), (201), (004), (202), respectively. These indices demonstrate the wurtzite structure of ZnO, which is composed of hexagonal cross-sections, JCPDS (File no: 043–0002).[53] The presence of sharp, narrow peaks indicates that the synthesised ZnO NPs are highly crystalline; furthermore, the intense peak exhibited at $2\Theta = 36°$ suggests the preferred growth orientation is along the (101) plane.[53] A study by Gurushankar et al. reported a ZnO-PVP diffraction pattern which is consistent with the XRD data in the current investigation. Moreover, this research group explains that high crystallinity is due to the formation of larger nanocrystals.[54] Figure 3(b) presents an XRD pattern of FeO-PVP NPs, where there are ten peaks with $2\Theta = 24°$, 33°, 35°, 40°, 49°, 54°, 57°, 62°, 63°, and 71° that correspond to (012), (104), (110), (113), (024), (116), (122), (214), (300) and (1010) planes, respectively. All peaks were indexed using JCPDS (File no. 89–0598), which revealed that the synthesised product represents the hematite (Fe_2O_3) phase of iron oxide.[55] Furthermore, the intense diffraction at $2\Theta = 35°$ demonstrates that the preferred growth is along the (104) plane.[55] The XRD analysis in the present work correlates to a study conducted by Guo *et al.*, where one of the aims was to synthesise hematite NPs using a mild hydrothermal method with PVP acting as a capping agent.

Figure 3(c) shows square-like NPs for PVP-capped FeO NPs, which correlates to the TEM data, however, the individual NPs assembled in clusters. The EDS spectrum of FeO-PVP NPs reveals a high purity of Fe with a weight percentage of 72.74%. Figure 2(d) reveals polydispersed, diamond-like NPs, correlating to the TEM observations. The EDS spectrum illustrates the Fe and O peaks with a total weight percentage of 78.57%, indicating an above-average purity in the synthesised sample. An FT-IR analysis was used to identify the functional groups present in metal oxide NPs. Figure 4(a) illustrates a comparative IR spectrum of PVP and ZnO-PVP NPs, where all the signature peaks of PVP are present in the IR spectrum of ZnO NPs. The broad, intense peak exhibited at 3426 cm^{-1} represents the O–H stretching vibration, which is due to adsorbed water by the particle's exterior surface.[57] The remaining four peaks are observed to have decreased in intensity, as well as a shift in peak position. The absorption peaks at 2972 cm^{-1}, 1626 cm^{-1}, 1509 cm^{-1}, and 1381 cm^{-1} correspond to the C–H, C=O, CH_2, and C–N vibrational groups in the pure PVP IR spectra.[57] The decreased peak intensity could be attributed to the calcination process, which could potentially reduce the concentration of

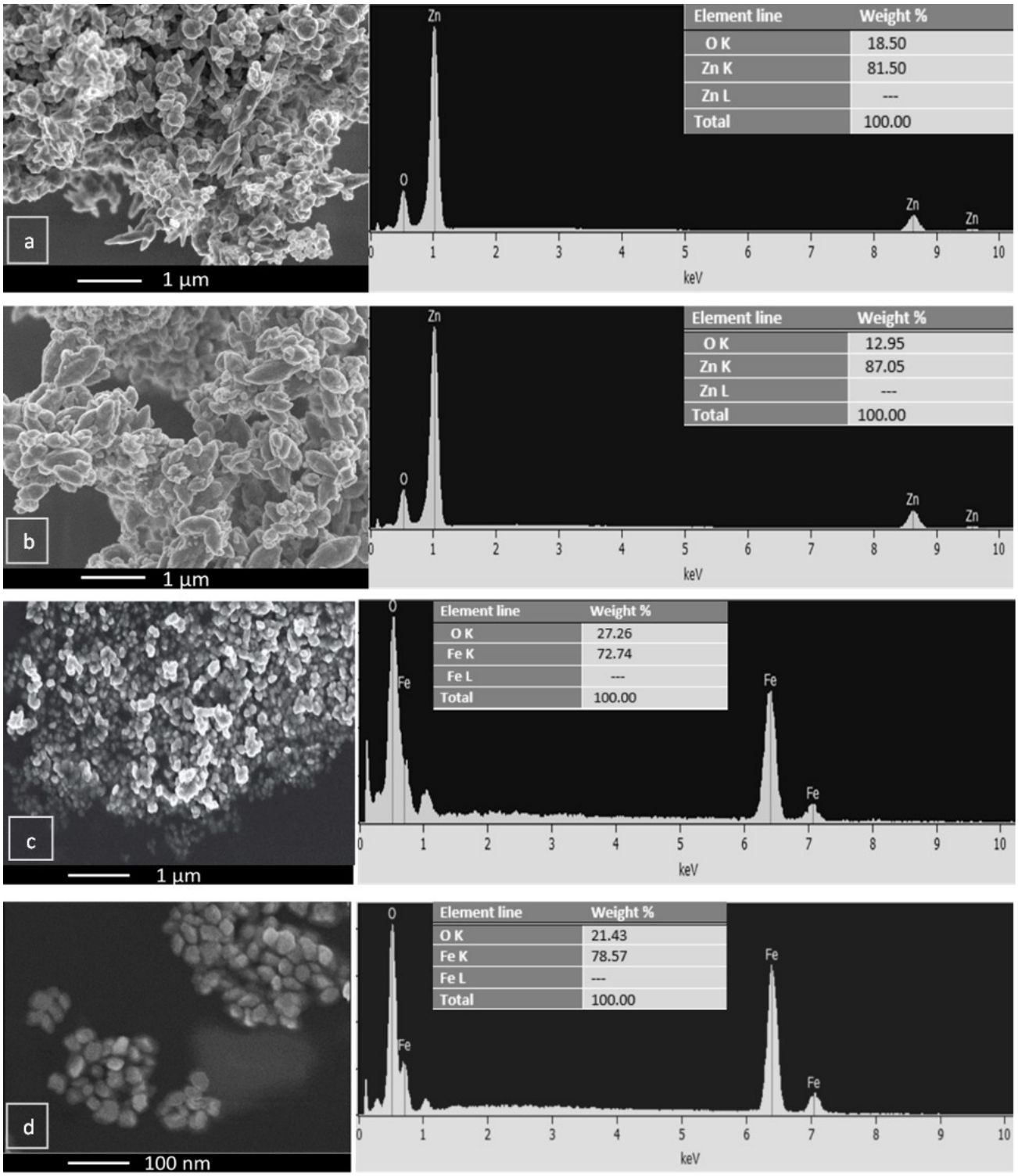

Figure 2. Morphology and size analyses of NPs: (a) PVP-capped ZnO, (b) CBD-capped ZnO, (c) PVP-capped FeO, (d) CBD-capped FeO.

PVP present on the surface of ZnO NPs. Rao *et al.* conducted a study that investigated the thermal decomposition of PVP, and the findings indicate that PVP starts to degrade at 250 °C and reaches 50 % degradation at 420 °C.[58] A peak shift represents a chemical interaction between PVP molecules and the surface molecules of ZnO; this is a result of ZnO NPs co-ordinating with the nitrogen and oxygen atoms in PVP.[57]

Figure 4(b) shows the FT-IR spectrum of the synthesised FeO-PVP NPs, where four characteristic peaks of PVP can be observed, indicating successful capping of FeO NPs with PVP.

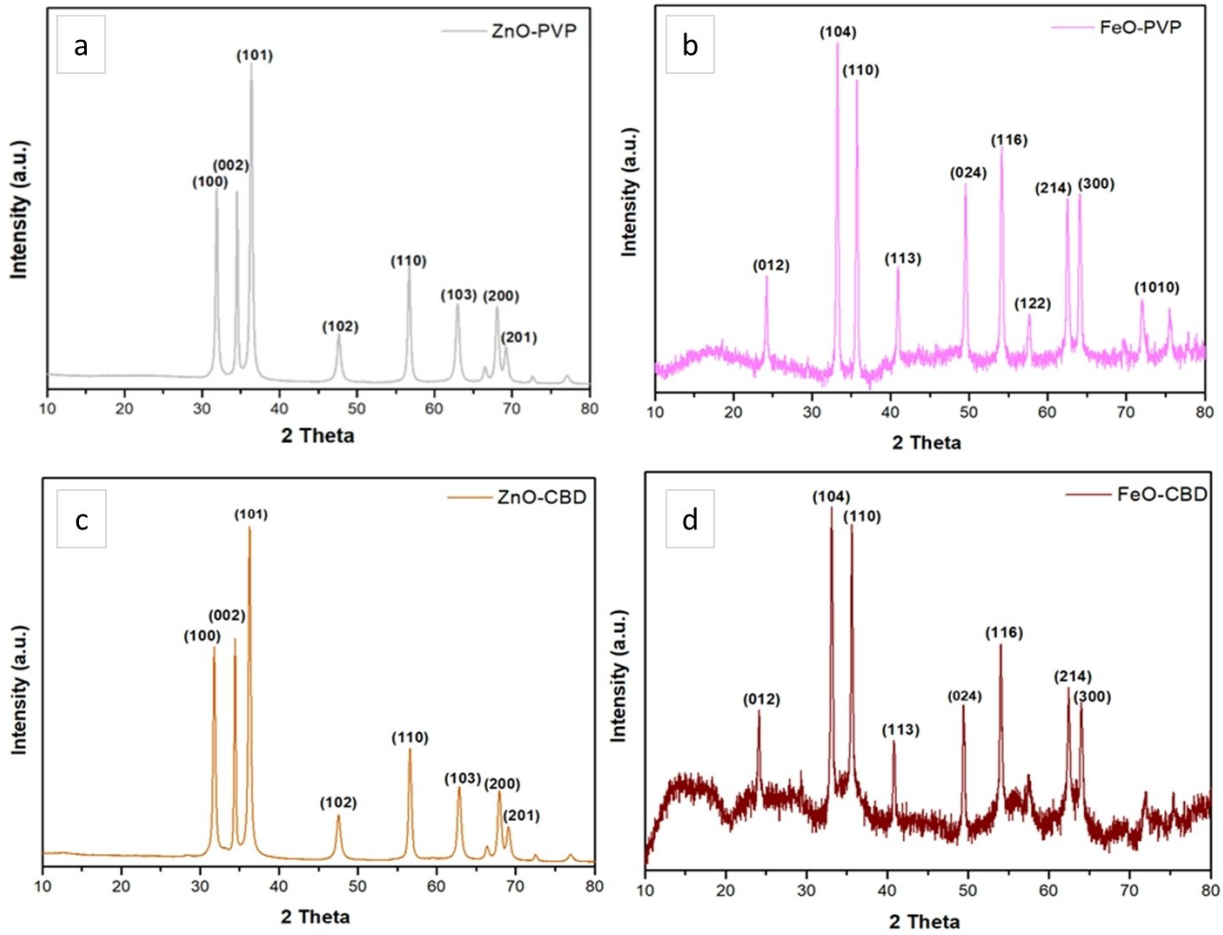

Figure 3. Structural analyses of NPs: (a) PVP-capped ZnO, (b) PVP-capped FeO, (c) CBD-capped ZnO, and (d) CBD-capped FeO.

The FT-IR analysis is consistent with previous literature.[59] An intense peak at 3359 cm^{-1} correlates to the O–H group in pure PVP. The absorption peak at 1612 cm^{-1} suggests that a chemical bond is formed between PVP and FeO NPs by the C=O group.[59] The decrease in peak intensity could be due to the calcination that the sample was subjected to, resulting in a decreased quantity of PVP in the sample. The FT-IR spectrum of ZnO-CBD NPs, reported in Figure 4(c), illustrates the characteristic peaks of CBD, which suggest successful capping of the synthesised product. The IR peaks at 3400 cm^{-1}, 2928 cm^{-1}, 1630 cm^{-1}, 1511 cm^{-1}, 1381 cm^{-1}, and 1039 cm^{-1} correspond to the O–H stretch, C–H stretch, C=C stretch, C–H bend, C–H wag, and C–O stretch in the CBD spectra.[60] A study by Alamdari *et al.*,[61] investigated the synthesis of ZnO NPs using a leaf extract of *Sambucus ebulus* and reported similar IR peaks in comparison to the ZnO NPs reported in the current work. In addition, the study explained that a shift or change in peak position or intensity indicates an interaction between the functional groups present in polyphenolic compounds and the ZnO NPs. Therefore, the peak shift and peak intensity reduction observed in Figure 4(c) suggest that the biomolecules present in CBD were capped or bonded onto the ZnO NP surface.

Figure 4(d) shows an IR spectrum of FeO-CBD NPs, where four characteristic peaks of CBD can be observed in FeO-CBD NPs, indicating successful capping of FeO-NPs with CBD. The IR peaks at 3421 cm^{-1}, 2922 cm^{-1}, 1625 cm^{-1} and 1397 cm^{-1} correspond to O–H, C–H stretching, C=C, and C–H bending vibrational groups.[62] A similar trend of peak intensity reduction, with a slight peak shift is observed in biosynthesised FeO NPs, which imply a chemical interaction between the biomolecules and the FeO NPs.[61]

In assessing PVP and CBD capping efficiencies, TEM analysis revealed distinct morphologies of PVP and CBD-capped NPs. The PVP-capped ZnO NPs displayed rectangles, nanocubes, and spheres, while CBD-capped ZnO NPs exhibited bulky elliptical disks and spheres, implying broader size variation. For FeO NPs, PVP-capped particles were polydispersed with square and flake-like structures. In contrast, CBD-capped FeO NPs displayed diamond-like shapes with minimal aggregation. Comparatively, PVP led to diverse NP morphologies, which is consistent with prior studies. CBD induced distinct precipitation behaviours and NP shapes due to its phenolic compounds, whereas PVP maintained uniform shapes through its stabilising influence. The FT-IR analysis highlights the distinctions between PVP and CBD as capping agents. Both agents show characteristic peaks in their respective IR spectra, confirming successful capping. However, variations in peak intensity, position shifts, and

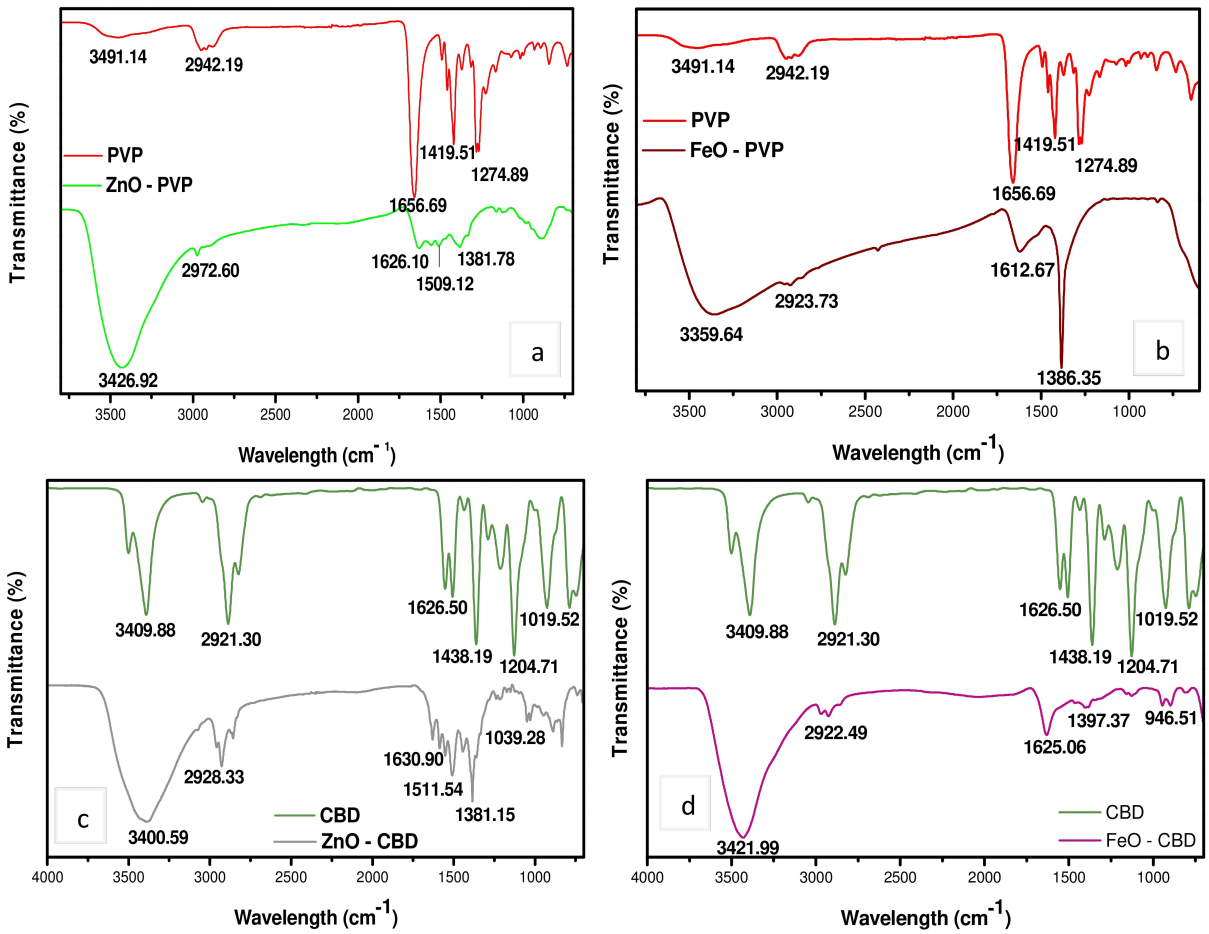

Figure 4. Molecular analyses of NPs: (a) PVP-capped ZnO, (b) PVP-capped FeO, (c) CBD-capped ZnO, (d) CBD-capped FeO.

specific vibrational groups denote differences attributed to the capping agent's chemistry and interaction with MONPs.

In general, capping agents, when used in synthesis, act as stabilisers through steric hindrance that counteract the agglomeration of NPs (thereby enhancing their dispersibility and shelf-life in final drug formulations), modify the biological activity and surface chemistry and alter the interaction of NPs inside the preparation medium.[63–65] In addition, capping agents sometimes augment the reduction kinetics of NPs by forming complex structures with the metallic ions in the precursor salts.[66] The plant-based bio constituents like terpenoids, polyols, alkaloids, polysaccharides, flavonoids, phenolics, proteins, amino acids, enzymes, etc., are reported to serve as strong chelating, reducing, and stabilising agents while playing an important role in tuning the shape and size of the NPs.[67] The presence of phytochemicals on the NP surface, in some instances, can alter their wettability and surface chemistry, providing enriched surfaces for cellular uptake and toxicity and contributing to the functionality, for instance, antimicrobial and anticancer activity.[68]

Cytotoxicity Analyses

To assess the cytotoxic potential of CBD-capped MONPs, a half-maximum inhibitory concentration (IC_{50}) investigation was conducted on HaCaT cell lines and results are reported in Table 1. Metal oxides capped with PVP were used as reference materials in this study. Increasing concentrations of PVP/CBD-capped metal oxide NPs (6.25 to 100 μg/mL) were evaluated against the HaCaT cell lines over 48 hours. In a prior study, our research group reported that CBD tested over a concentration range (2.2 to 200 μM) exhibited an IC_{50} of 5.82 ± 1.06 μM when exposed to HaCat cells over 48 hours.[69] To the author's knowledge, no previous research papers have evaluated CBD-capped metal oxide NPs for cytotoxicity against HaCaT cells.

Within the concentration range of 6.25 to 100 μg/mL, both the reference materials and the FeO-NPs capped with CBD demonstrated no discernible cytotoxic effects on HaCaT cells. Conversely, the CBD-capped ZnO-NPs exhibited a modest level of toxicity within the aforementioned concentration range, leading to a near-50% reduction of cell density at 100 μg/mL. Hammel *et al.*[70] explored the effectiveness of topically applied CBD (1–10%) in a gel formulation for alleviating inflammation-associated symptoms in a monoarthritic rat model. The rats were administered doses of 0.6, 3.1, and 6.2 mg/day, which

Table 1. The IC_{50} values of polyvinylpyrrolidone/cannabidiol-capped metal oxide nanoparticles in human keratinocyte cells.

Drug compound	IC_{50}[a] ± SEM[b] on HaCaT[c] (μg/mL or μM[h])	Cell density (%) at highest concentration tested (100 μg/mL or 200 μM[h])
ZnO[d]-PVP[e]	> 100	62.86 ± 9.23
FeO[f]-PVP	> 100	75.28 ± 8.91
ZnO-CBD[g]	> 100	52.41 ± 2.62
FeO-CBD	> 100	133.72 ± 8.20
CBD	5.82 ± 1.06	11.68 ± 2.03

[a]Half maximal inhibitory concentration, [b]Standard error of the mean, [c]Cultured human keratinocyte cells, [d]Zinc oxide, [e]Polyvinylpyrrolidone, [f]Iron oxide, [g]Cannabidiol, [h]Nanoparticles in μg/mL and isolated compounds in μM.

exhibited a strong linear relationship.[70] The concentration of CBD applied transdermally in their study far exceeded our tested concentration range, and there were no reported adverse effects on keratinocytes. Therefore, despite our findings indicating a marginal reduction in cell density, it can be reasonably considered safe for use in a topical formulation in animal studies.

In the context of biological systems, the constituents of a biological medium can influence NPs, particularly through protein absorption, leading to the formation of protein-coated NPs.[71] The process of protein-coating introduces modifications to the surface charge, dispersion, size, biodistribution, and biological effects of NPs, which can have either beneficial or detrimental implications depending on the intended purpose.[72] In this study, NPs were dispersed in Dulbecco's Modified Eagle Medium (DMEM) before exposure to cells, which introduces the possibility of altering their biological properties.

The TEM images in Figure 5(a) and (b) depict FeO NPs capped with CBD and PVP, respectively. Upon dispersion in DMEM, a noticeable structural alteration was observed. However, the primary observation of significance was the presence of a substantial protein coating enveloping the NPs, which could explain the absence of cytotoxicity in HaCaT cells.

The FeO NPs exhibit an augmented coating, leading to an increase in particle size, which may potentially reduce cellular uptake of the NP and subsequent cytotoxic effects. Conversely, ZnO NPs have transformed, assuming a spherical shape, which renders them smaller than their initial synthesised state. This alteration enhances the probability of cellular uptake. It is plausible that the observed cytotoxicity in ZnO CBD NPs may be attributed to the enhanced uptake of NP where CBD's effect is more pronounced, given the IC_{50} of 5.82 ± 1.06 of CBD on HaCaT cells.

Figures 5(c) and (d) present images of ZnO NPs capped with CBD and PVP, respectively. The morphology of the NPs has transitioned from elliptical disks and spheres to a spherical shape. Furthermore, the CBD-capped ZnO NPs display an average size of 52 nm and exhibit monodispersity, contrasting with the previously observed bulky and overlapping ZnO NPs with an average size of 90 nm. This particular characteristic may contribute to the observed cytotoxicity in HaCaT cells. Previous literature suggests that smaller NPs have a higher propensity for cellular uptake.[73] Furthermore, a study by Augustine *et al.*,[74] indicates the influence of particle size on release kinetics and bio-distribution. This phenomenon can be attributed to the observation that NPs are less likely to trigger an immune response as foreign bodies when compared to larger micro and macro-sized particles. A paper by Ottemann *et al.*,[75] *reveals that NP morphology also affects the* cellular uptake of nanomaterials and subsequent cellular functions. In addition, elongated nanomaterials exhibit an increased uptake in comparison to spherical counterparts, due to the enhanced cell membrane adhesion. According to a study by Liao *et al.*[76] in 2020, the cellular internalisation of ZnO-NPs *in-vitro* are attributed to the diffusion of Zn^{2+} ions through the cell membrane.[76] Subsequently, NP penetration into the cytoplasm is facilitated, leading to the generation of reactive oxygen species (ROS). These ROS molecules interrupt the normal functioning of proteins, DNA molecules, and the mitochondria. This triggers a cascade effect, inducing oxidative stress in the endoplasmic reticulum (ER) and eventually culminating in cell death.[77] Lee *et al.*[78] studied the toxic effect of 22 ± 5 nm spherical ZnO NPs on HaCaT cells and found a significant decrease in cell viability through ROS generation and oxidative stress at 40 μg/mL or higher. On the other hand, Zanni and co-workers investigated the cytotoxicity of zinc oxide nanorods (ZnO-NR) with diameters ranging from 20–40 nm and lengths up to 4 μm on HaCaT cells and reported a very low cytotoxic effect at the highest tested concentration of 100 μg/mL, which indicates the effect of NP shape and size on cytotoxicity.[79] Wu *et al.*[80] suggested a cytotoxic concentration of ZnO NPs between 30–50 μg/mL for the HaCaT cell line in DMEM. Surface modification of ZnO NPs via functionalisation, coating or adsorption of components from supplemented cell culture medium are reported to reduce the toxicity of the NPs.[81]

Conclusions

This study has successfully synthesised and characterised MONPs using CBD and PVP as capping agents. The results demonstrated the cytotoxic effects of CBD-capped ZnO NPs on HaCaT cells, while CBD-capped FeO NPs and PVP-capped MONPs exhibited no noticeable cytotoxicity. The presence of protein coatings on the NPs dispersed in a biological medium is believed to play a role in the observed cytotoxicity and its

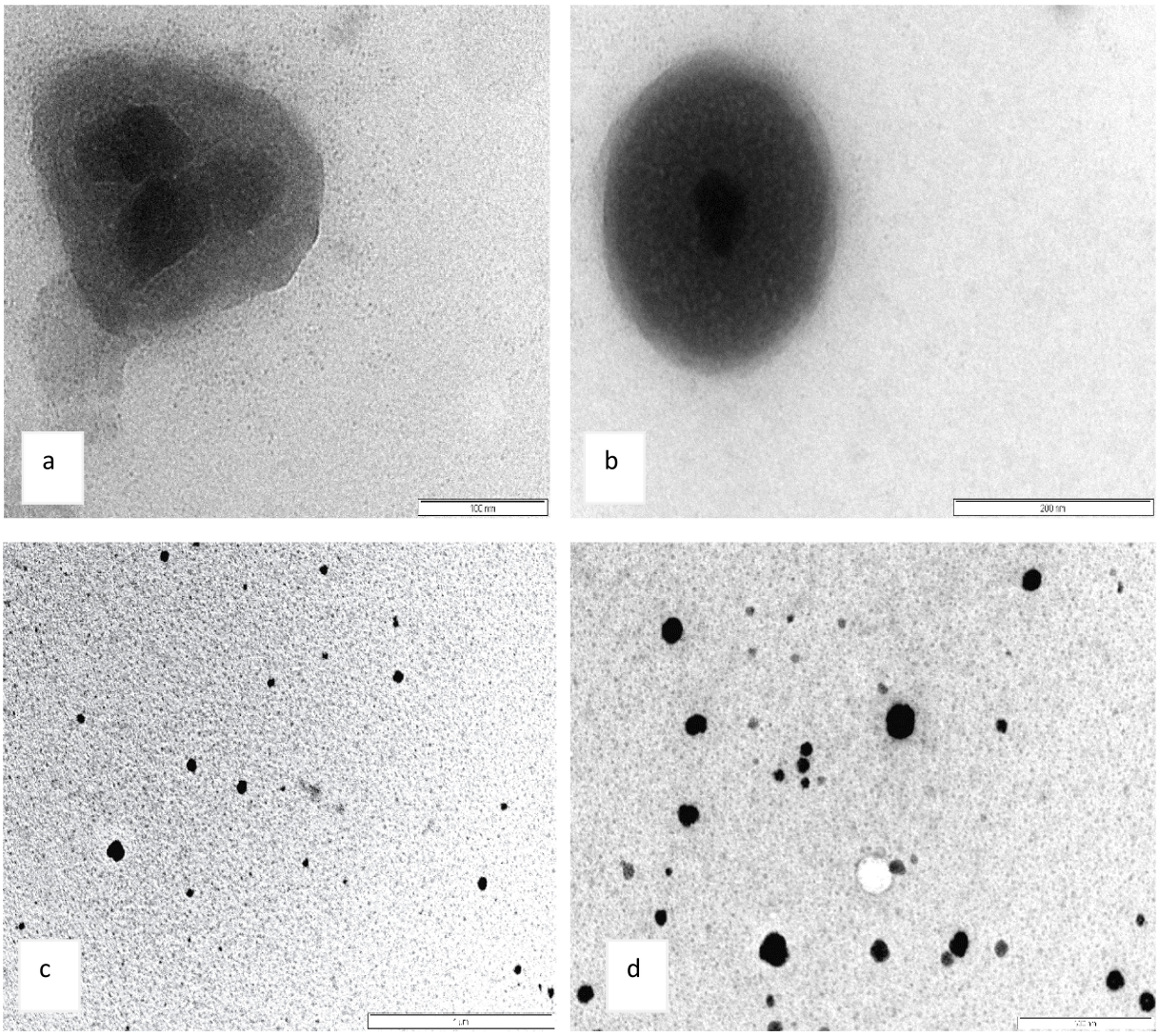

Figure 5. Metal oxides dispersed in Dulbecco's Modified Eagle Medium; (a) CBD-capped FeO, (b) PVP-capped FeO, (c) CBD-capped ZnO, (d) PVP-capped ZnO.

absence. These findings contribute to the knowledge and understanding of the potential applications of nanobiotechnology in the fields of dermato-cosmetics and transdermal drug delivery.

Further investigations are required to understand the mechanisms responsible for the cytotoxicity induced by CBD-capped ZnO NPs and to elucidate the influence of protein coatings on cellular responses. Exploring alternative capping and reducing agents, as well as different synthesis methods, could provide valuable insights into optimising MONPs for diverse biomedical applications. Moreover, conducting *in-vivo* studies is imperative to assess the safety and efficacy of these NPs in more complex biological systems. This study paves the way for future research endeavours in nanobiotechnology, with the potential development of treatments for skin disorders and advancements in drug delivery systems.

Experimental Section

Materials for Nanoparticle Synthesis

All materials employed in the chemical synthesis were of analytical grade and were utilised without further purification. The materials included: zinc nitrate ($Zn(NO_3)_2$) (Minema Chemicals, South Africa), polyvinylpyrrolidone (PVP) (Sigma Aldrich, South Africa), ferric nitrate nonahydrate ($Fe(NO_3)_3$) (Sisco Research Laboratories, India), ethanol (99%) (EthanolSA, South Africa), sodium hydroxide (NaOH) (Minema Chemicals, South Africa) and CBD crystals (99%) (Endoca BV, Netherlands) kindly supplied by BGM Pharmaceuticals, South Africa, deionised (DI) water (CSIR, South Africa). The optimisation of MONPs in this study involved several parameter variations (Table 2–4).

Microwave-assisted Chemical and Green Synthesis of MONPs

Synthesis of MONPs followed a similar method outlined by Barreto *et al.*[82], however, the current work incorporated slight alterations. The ZnO and FeO NPs were synthesised employing $Zn(NO_3)_2$ and $Fe(NO_3)_3$ as the respective precursor salts. A 0.1 M solution of each

Table 2. Optimisation parameters for synthesised nanoparticles.

Capping agent PVP[a] (g)	Concentration of CBD[b] (M)	Volume of capping reagent solution (mL)	Volume of 0.1 M precursor salt (mL)	Synthesis time (min)	Synthesis temp (°C)	pH	Calcination temp (°C)
0.5	0.00025	40	1, 2 or 5	30	100	9	525
0.25	0.001	25	10	20	70	8	400
0.1	0.01	10	25	10	50	7	300

[a]Polyvinylpyrrolidone; [b]Cannabidiol

Table 3. Optimised parameters for PVP-capped nanoparticles.

Nanoparticle	Concentration of precursor salt (M)	Volume of precursor salt (mL)	PVP[a] (g)	Synthesis time (min)	Synthesis temp (°C)	pH	Calcination temp & time (°C)
ZnO[b]	0.1	25	0.5	30	100	9	4 hrs @ 400
FeO[c]	0.1	25	0.5	30	100	8	3 hrs @ 400

[a]Polyvinylpyrrolidone; [b]Zinc oxide; [c]Iron oxide

Table 4. Optimised parameters for CBD-capped nanoparticles.

Nanoparticle	Concentration of precursor salt (M)	Volume of precursor salt (mL)	Concentration of CBD[a] (M)	Volume of CBD (mL)	Synthesis time (min)	Synthesis temp (°C)	pH
ZnO[b]	0.1	25	0.01	10	30	100	8
FeO[c]	0.1	25	0.001	10	30	100	8

[a]Cannabidiol; [b]Zinc oxide; [c]Iron oxide

salt was prepared by dissolution in deionised (DI) water. A 0.2 M NaOH solution was gradually added to this solution under magnetic stirring at room temperature (25 °C) until the desired pH was achieved. Subsequently, solutions of PVP or CBD, with increasing concentrations, were incorporated and stirred for an additional 10 minutes at room temperature (25 °C) prior to transferring the mixture to a Teflon-coated vessel. The synthesis reactions were conducted within a microwave reactor (Milestone Ultraclave MA033, USA) with varying parameters of time and temperature. The resulting precipitate underwent washing using DI water and then ethanol, followed by centrifugation at 1,917 RCF using the Rotofix 32 A (Hettich, USA) centrifuge, repeated 3 to 4 times. The obtained precipitate was then dried in a vacuum oven at 100 °C for 24 hours, after which it was subjected to calcination in a muffle furnace at increasing temperatures. The CBD-capped NPs were exempt from calcination due to potential degradation at elevated temperatures. The final product was crushed into a fine powder using a quartz mortar and pestle, sieved to a particle size of 75 μm, and stored in a sealed container at room temperature for subsequent analyses.

Characterisation of NPs

Within the field of material science, characterisation is defined as a process employed to investigate the properties and structure of a synthesised material. This role of characterisation is crucial in confirming that the synthesised particles are within the nanoscale range.[83] In NP characterisation, the two primary parameters examined are morphology and size, followed by an evaluation of the crystalline structure and chemical composition of the nanoparticles.[84]

Transmission Electron Microscopy (TEM) generates lateral spatial high-resolution micrographs and diffraction patterns[85] by directing an electron beam onto a sample and hence has the capability of investigating the shape, size, and crystal structure of a NP.

This study employed a JEOL TEM-2100 (JEOL, Japan) for sample analyses. Sample preparation involved dispersing a small quantity of powder sample in ethanol (~1 mL), followed by 20 minutes of sonication. A copper grid was immersed in this mixture and left to air dry. The prepared copper grid was fixed onto a sample holder and inserted into the microscope for image capturing and subsequent analysis.

The Scanning Electron Microscope (SEM) captures micrographs of a sample's surface structure by detecting secondary electrons emitted when the sample interacts with the electron beam.[86] Within the SEM, an integrated feature called energy-dispersive X-ray spectroscopy (EDS) allows for the acquisition of elemental analysis data from the samples. A JEOL-JSM 7500F (JEOL, Japan) SEM was used to analyse the NP samples. Samples were prepared by dispersing a minute amount of powdered sample onto a conductive carbon tape, which was adhered to a stub. The stub was inserted into the microscope and images were captured. Element analysis was facilitated using the NSS software tool.

X-ray diffraction (XRD) is a technique that analyses Bragg's Law of reflection to investigate the structural characteristics of a sample. The Bragg peaks in an XRD pattern represent unique crystallographic orientations.[87] In this study, the crystalline structure of NPs was analysed using powder X-ray diffraction (PXRD) and recorded using a PAnalytical XPERT-PRO diffractometer (PAnalytical, Netherlands). A small amount of powdered sample was placed on a sample holder, smoothed out, and inserted into the XRD chamber for analysis.

Fourier-transform infrared spectroscopy (FTIR) assesses the transmission or absorption of infrared radiation across different wave-

lengths in a sample. This infrared absorption function facilitates the identification of functional groups and molecular structures within a sample.[88] This study employed a Spectrum 100 FTIR spectrometer (PerkinElmer, USA) to identify organic compounds in the sample. A powdered sample was affixed to the sample holder and compressed into a pellet, where sample measurements were then acquired.

Materials for Cytotoxicity Evaluation

The materials utilised for cell culture in this study are consistent with those detailed in a prior investigation conducted by our research team.[69]

Cell Culture

The maintenance of HaCaT cell lines followed the protocol described in a preceding study conducted by our research team.[69]

Sulforhodamine B Staining

The HaCaT cells (100 μL) were seeded in a 96-well microtitre plate. The plate was incubated for 24 hours at 37°C and 5% CO_2 to allow the cells to attach to the plate surface. The NPs were each prepared to a stock solution of 0.6 mg/mL and were filtered using a sterile syringe filter (0.2 μm). Cells were exposed to 100 μL medium (negative control), DMSO (0.8%; vehicle control), or NPs (6.25 to 100 μg/mL) prepared in FBS-free medium for 48 hours. A row of blanks (5% FBS-supplemented medium) was also allocated on each plate to account for sterility and background noise. After exposure, 50 μL of 50% TCA was added to each well and incubated at 4°C for a further 24 hours to fix the cells. Thereafter, TCA was washed off with tap water and allowed to air dry. A volume of 100 μL of SRB dye (0.057% in 1% acetic acid) was added to each well, and the plate was incubated for 1 hour. The unbound SRB dye was washed off with 100 μL 1% acetic acid thrice, and the plates were allowed to dry. Tris-buffer solution (200 μL; 10 mM, pH 10.5) was added to all wells to solubilise the bound dye. Plates were measured spectrophotometrically using an ELX 800 plate reader (BioTek Industries) at 540 nm (reference wavelength = 630 nm). Values were blank-excluded, and the cell density was calculated using the following formula;

$$\textit{Cell density}\ (\%\ \textit{of negative control}) = \left(\frac{\textit{absorbance of sample}}{\textit{average absorbance of negative control}}\right) X\ 100$$

The assay was performed with technical and biological triplicates. GraphPad Prism software was employed for statistical analysis of the half-maximal inhibitory concentration (IC_{50}).

Author Contributions

Experimental work, conceptualisation, and preparation of original draft (AJJ and WCC). Provided expert opinion and critical review (SSR, SKP and NLL). Provided technical expertise for cytotoxicity analysis (MN and DT)

Acknowledgements

The authors (SSR, AJJ, SKP) would like to thank the Department of Science and Innovation (C6ACH77) and the Council for Scientific and Industrial Research (086ADMI) for financial support. The authors thank Tautomer Biosciences for providing the drug (CBD) required to conduct this study.

Conflict of Interests

The authors declare no conflict of interest

Data Availability Statement

The data that support the findings of this study are available from the corresponding author upon reasonable request.

Keywords: Cannabidiol · Cytotoxicity · Metal Oxide Nanoparticles · Microwave-Assisted Synthesis · Material Characterisation

[1] T. Deka, M. K. Das, S. Das, L. R. Singha, P. Das, *Nano Medicine and Nano Safety*, Springer, Singapore, **2020**, 3–25.
[2] T. A. Saleh, V. K. Gupta, *Nanomaterial and Polymer Membranes*, Elsevier, **2016**, 83–133.
[3] Z. Yu, L. Tetard, L. Zhai, J. Thomas, *Energy Environ. Sci.* **2015**, *8*, 702–730.
[4] F. Matteucci, R. Giannantonio, F. Calabi, A. Agostiano, G. Gigli, M. Rossi, in *AIP Conf. Proc.*, American Institute Of Physics Inc., **2018**.
[5] S. Parveen, R. Misra, S. K. Sahoo, *Nanomedicine* **2012**, *8*, 147–166.
[6] L. A. Delouise, *J. Invest. Dermatol.* **2012**, *132*, 964–975.
[7] S. Pan, T. B. Goudoulas, J. Jeevanandam, K. X. Tan, S. Chowdhury, M. K. Danquah, *Front. Bioeng. Biotechnol.* **2021**, *9*, 724499.
[8] D. H. Sur, M. Mukhopadhyay, *Bioprocess Biosyst. Eng.* **2019**, *42*, 187–198.
[9] M. A. Abomuti, E. Y. Danish, A. Firoz, N. Hasan, M. A. Malik, *Biology (Basel)* **2021**, *10*, 1075.
[10] R. Motazedi, S. Rahaiee, M. Zare, *Bioorg. Chem.* **2020**, *101*, 103998.
[11] A. ur R. Khan, K. Huang, Z. Jinzhong, T. Zhu, Y. Morsi, A. Aldalbahi, M. El-Newehy, X. Yan, X. Mo, *J. Mater. Chem. B* **2021**, *9*, 1452–1465.
[12] A. Czyżowska, A. Barbasz, *Int. J. Environ. Health Res.* **2022**, *32*, 885–901.
[13] N. Abbasi Aval, J. Pirayesh Islamian, M. Hatamian, M. Arabfirouzjaei, J. Javadpour, M.-R. Rashidi, *Int. J. Pharm.* **2016**, *509*, 159–167.
[14] M. F. Attia, N. Anton, I. U. Khan, C. A. Serra, N. Messaddeq, A. Jakhmola, R. Vecchione, T. Vandamme, *Int. J. Pharm.* **2016**, *508*, 61–70.
[15] E. Maltas, M. Ozmen, B. Yildirimer, S. Kucukkolbasi, S. Yildiz, *J. Nanosci. Nanotechnol.* **2013**, *13*, 6522–6528.
[16] W. Y. Jeong, M. Kwon, H. E. Choi, K. S. Kim, *Biomaterials* **2021**, *25*, 1–15.
[17] D. Ramadon, M. T. C. McCrudden, A. J. Courtenay, R. F. Donnelly, *Drug Delivery Transl. Res.* **2022**, *12*, 758–791.
[18] F. Sabbagh, B. S. Kim, *J. Controlled Release* **2022**, *341*, 132–146.
[19] H. Tanwar, R. Sachdeva Guru Jambheshwar, *Int. J. Pharm. Sci. Res.* **2016**, *7*, 2274.
[20] U. Bagul, S. Biyani, **2019**, DOI: 10.5281/zenodo.3475021.
[21] R. Abu-Huwaij, M. M. Abbas, R. Al-Shalabi, F. N. Almasri, *Appl. Nanosci.* **2022**, *12*, 69–78.
[22] V. Raviraj, B. T. T. Pham, B. J. Kim, N. T. H. Pham, L. F. Kok, N. Painter, N. C. Delic, S. K. Jones, B. S. Hawkett, J. G. Lyons, *Cancer Nanotechnol.* **2021**, *12*, DOI: 10.1186/s12645-021-00079-7.
[23] L. A. F. Afiune, C. Y. Ushirobira, D. P. P. Barbosa, P. E. N. de Souza, M. I. G. Leles, M. Cunha-Filho, G. M. Gelfuso, M. A. G. Soler, T. Gratieri, *Int. J. Pharm.* **2020**, *587*, 119709.
[24] L. Liu, W. Zhao, Q. Ma, Y. Gao, W. Wang, X. Zhang, Y. Dong, T. Zhang, Y. Liang, S. Han, J. Cao, X. Wang, W. Sun, H. Ma, Y. Sun, *Nanoscale Adv.* **2023**, *5*, 1527–1558.
[25] R. Javed, M. Zia, S. Naz, S. O. Aisida, N. U. Ain, Q. Ao, *J. Nanobiotechnol.* **2020**, *18*, 172.

[26] P. Sharma, S. Kumari, D. Ghosh, V. Yadav, A. Vij, P. Rawat, S. Kumar, C. Sinha, S. Saini, V. Sharma, M. I. Hassan, C. M. Srivastava, S. Majumder, *Mater. Chem. Phys.* **2021**, *258*, 123899.
[27] A. K. Sidhu, N. Verma, P. Kaushal, *Front. Nanotechnol.* **2022**, *3*, DOI: 10.3389/fnano.2021.801620.
[28] V. Martínez, A. Iriondo De-Hond, F. Borrelli, R. Capasso, M. D. del Castillo, R. Abalo, *Int. J. Mol. Sci.* **2020**, *21*, 3067.
[29] K. M. Nelson, J. Bisson, G. Singh, J. G. Graham, S.-N. Chen, J. B. Friesen, J. L. Dahlin, M. Niemitz, M. A. Walters, G. F. Pauli, *J. Med. Chem.* **2020**, *63*, 12137–12155.
[30] D. Wu, J. Zhou, M. N. Creyer, W. Yim, Z. Chen, P. B. Messersmith, J. V. Jokerst, *Chem. Soc. Rev.* **2021**, *50*, 4432–4483.
[31] P. Sathishkumar, F. L. Gu, Q. Zhan, T. Palvannan, A. R. Mohd Yusoff, *Mater. Lett.* **2018**, *210*, 26–30.
[32] B. G. Anand, K. Dubey, D. S. Shekhawat, K. Kar, *Biochemistry* **2016**, *55*, 3345–3348.
[33] A. M. El Shafey, *Green Process. Synth.* **2020**, *9*, 304–339.
[34] E. Shaabani, S. M. Amini, S. Kharrazi, R. Tajerian, *Nanomed. J.* **2017**, *4*, 115–125.
[35] D. L. Almeida, L. A. Devi, *Pharmacol. Res. Perspect.* **2020**, *8*, e00682.
[36] S. Petrosino, R. Verde, M. Vaia, M. Allarà, T. Iuvone, V. Di Marzo, *J. Pharmacol. Exp. Ther.* **2018**, *365*, 652–663.
[37] S. M. Baswan, A. E. Klosner, K. Glynn, A. Rajgopal, K. Malik, S. Yim, N. Stern, *Clin. Cosmet. Investig. Dermatol.* **2020**, *13*, 927–942.
[38] B. P. Ferreira, G. Costa, F. Mascarenhas-Melo, P. C. Pires, F. Heidarizadeh, P. S. Giram, P. G. Mazzola, C. Cabral, F. Veiga, A. C. Paiva-Santos, *Phytochem. Rev.* **2023**, *22*, 781–828.
[39] B. Ni, Y. Liu, M. Dai, J. Zhao, Y. Liang, X. Yang, B. Han, M. Jiang, *Biomed. Pharmacother.* **2023**, *165*, 115074.
[40] M. Graczyk, A. A. Lewandowska, T. Dzierżanowski, *Molecules* **2021**, *26*, 4551.
[41] S. V. Jadhav, D. S. Nikam, V. M. Khot, N. D. Thorat, M. R. Phadatare, R. S. Ningthoujam, A. B. Salunkhe, S. H. Pawar, *New J. Chem.* **2013**, *37*, 3121.
[42] G. Lu, S. Li, Z. Guo, O. K. Farha, B. G. Hauser, X. Qi, Y. Wang, X. Wang, S. Han, X. Liu, J. S. DuChene, H. Zhang, Q. Zhang, X. Chen, J. Ma, S. C. J. Loo, W. D. Wei, Y. Yang, J. T. Hupp, F. Huo, *Nat. Chem.* **2012**, *4*, 310–316.
[43] K. M. Koczkur, S. Mourdikoudis, L. Polavarapu, S. E. Skrabalak, *Dalton Trans.* **2015**, *44*, 17883–17905.
[44] J. Lakey-Beitia, A. M. Burillo, G. La Penna, M. L. Hegde, K. S. Rao, *J. Alzheimer's Dis.* **2021**, *82*, S335–S357.
[45] L. E. Romo, H. Saade, B. Puente, M. L. López, R. Betancourt, R. G. López, *J. Nanomater.* **2011**, *2011*, 145963.
[46] D. P. Joshi, G. Pant, N. Arora, S. Nainwal, *Heliyon* **2017**, *3*, e00253.
[47] A. P. A. Oliveira, J. F. Hochepied, F. Grillon, M. H. Berger, *Chem. Mater.* **2003**, *15*, 3202–3207.
[48] H. Kamari, N. Al-Hada, E. Saion, A. Shaari, Z. Talib, M. Flaifel, A. Ahmed, *Crystals (Basel)* **2017**, *7*, 2.
[49] X. Huang, M. G. Willinger, H. Fan, Z. L. Xie, L. Wang, A. Klein-Hoffmann, F. Girgsdies, C. S. Lee, X. M. Meng, *Nanoscale* **2014**, *6*, 8787–8795.
[50] A. C. Ersan, M. Yildirim, A. S. Kipcak, N. Tugrul, *Acta Chim. Slov.* **2016**, *63*, 881–890.
[51] M. F. Silva, L. A. S. de Oliveira, M. A. Ciciliati, M. K. Lima, F. F. Ivashita, D. M. Fernandes De Oliveira, A. A. W. Hechenleitner, E. A. G. Pineda, *J. Nanomater.* **2017**, *2017*, 7939727.
[52] X. Yang, H. Sun, L. Zhang, L. Zhao, J. Lian, Q. Jiang, *Sci. Rep.* **2016**, *6*, 1–12.
[53] M. Shatnawi, A. M. Alsmadi, I. Bsoul, B. Salameh, M. Mathai, G. Alnawashi, G. M. Alzoubi, F. Al-Dweri, M. S. Bawa'aneh, *Results Phys.* **2016**, *6*, 1064–1071.
[54] K. Gurushankar, S. Jeyavijayan, M. Gohulkumar, K. Viswanathan, *Int. J. Chem. Sci.* **2018**, *16*, 1–7.
[55] M. Aliahmad, N. Nasiri Moghaddam, *Mater. Sci. Pol.* **2013**, *31*, 264–268.
[56] S. Thirumal, S. R. Senthilkumar, T. Sivakumar, *Int. J. Pharm. Sci.* **2014**, *6*, 461–465.
[57] T. Gutul, E. Rusu, N. Condur, V. Ursaki, E. Goncearenco, P. Vlazan, *Beilstein J. Nanotechnol.* **2014**, *5*, 402–406.
[58] V. Rao, P. Latha, P. V. Ashokan, M. H. Shridhar, *Polym. J.* **1999**, *31*, 887–889.
[59] D. Li, S. J. Li, Y. Zhang, J. J. Jiang, W. J. Gong, J. H. Wang, Z. D. Zhang, *Mater. Res. Innovations* **2015**, *19*, S58–S62.
[60] A. Brunning, "Compound Interest - Analytical Chemistry–Infrared (IR) Spectroscopy," can be found under http://www.compoundchem.com/2015/02/05/irspectroscopy/, **2015**.
[61] S. Alamdari, M. Sasani Ghamsari, C. Lee, W. Han, H.-H. Park, M. J. Tafreshi, H. Afarideh, M. H. M. Ara, *Appl. Sci.* **2020**, *10*, 3620.
[62] J. A. A. Abdullah, L. Salah Eddine, B. Abderrhmane, M. Alonso-González, A. Guerrero, A. Romero, *Sustain. Chem. Pharm.* **2020**, *17*, 100280.
[63] A. K. Sidhu, N. Verma, P. Kaushal, *Front. Nanotechnol.* **2022**, *3*, DOI: 10.3389/fnano.2021.801620.
[64] M. I. Din, A. Rani, Z. Hussain, R. Khalid, A. Aihetasham, M. Mukhtar, *Int. J. Environ. Anal. Chem.* **2021**, *101*, 821–837.
[65] S. Jadoun, R. Arif, N. K. Jangid, R. K. Meena, *Environ. Chem. Lett.* **2021**, *19*, 355–374.
[66] S. Campisi, M. Schiavoni, C. Chan-Thaw, A. Villa, *Catalysts.* **2016**, *6*, 185.
[67] C. V. Restrepo, C. C. Villa, *Environ Nanotechnol. Monit. Manag.* **2021**, *15*, 100428.
[68] K. T. Tadele, T. O. Abire, T. Y. Feyisa, *J. Nanomed.* **2021**, *4*, 1040.
[69] A. J. Josiah, S. K. Pillai, W. Cordier, M. Nell, D. Twilley, N. Lall, S. S. Ray, *ACS Omega* **2021**, *6*, 29078–29090.
[70] D. C. Hammell, L. P. Zhang, F. Ma, S. M. Abshire, S. L. McIlwrath, A. L. Stinchcomb, K. N. Westlund, *Eur. J. Pain.* **2016**, *20*, 936–948.
[71] R. Rampado, S. Crotti, P. Caliceti, S. Pucciarelli, M. Agostini, *Front. Bioeng. Biotechnol.* **2020**, *8*, DOI: 10.3389/fbioe.2020.00166.
[72] D. Nierenberg, A. R. Khaled, O. Flores, *Rep. Pract. Oncol. Radiother.* **2018**, *23*, 300–308.
[73] Y. Zhao, Y. Wang, F. Ran, Y. Cui, C. Liu, Q. Zhao, Y. Gao, D. Wang, S. Wang, *Sci. Rep.* **2017**, *7*, 1–11.
[74] R. Augustine, A. Hasan, R. Primavera, R. J. Wilson, A. S. Thakor, B. D. Kevadiya, *Mater. Today Commun.* **2020**, *25*, DOI: 10.1016/j.mtcomm.2020.101692.
[75] B. M. Ottemann, A. J. Helmink, W. Zhang, I. Mukadam, C. Woldstad, J. R. Hilaire, Y. Liu, J. M. McMillan, B. J. Edagwa, R. L. Mosley, J. C. Garrison, B. D. Kevadiya, H. E. Gendelman, *Biomaterials* **2018**, *185*, 174–193.
[76] C. Liao, Y. Jin, Y. Li, S. C. Tjong, *Int. J. Mol. Sci.* **2020**, *21*, 1–49.
[77] V. Sharma, D. Anderson, A. Dhawan, *Apoptosis* **2012**, *17*, 852–870.
[78] S. H. Lee, H. R. Lee, Y. R. Kim, M. K. Kim, *Toxicol. Environ. Health Sci.* **2012**, *4*, 14–18.
[79] E. Zanni, S. De Palma, C. R. Chandraiahgari, G. De Bellis, S. Cialfi, C. Talora, C. Palleschi, M. S. Sarto, D. Uccelletti, P. Mancini, *Mater. Lett.* **2016**, *179*, 90–94.
[80] Z. Wu, H. Yang, G. Archana, M. Rakshit, K. W. Ng, C. Y. Tay, *J. Nanotoxicol.* **2018**, *12*, 1215–1229.
[81] H. Yin, R. Chen, P. S. Casey, P. C. Ke, T. P. Davis, C. Chen, *RSC Adv.* **2015**, *5*, 73963–73973.
[82] G. P. Barreto, G. Morales, Ma. L. L. Quintanilla, *J. Mater.* **2013**, *2013*, 1–11.
[83] D. Titus, E. James Jebaseelan Samuel, S. M. Roopan, in *Green Synthesis, Characterisation and Applications of Nanoparticles*, Elsevier, **2018**, pp. 303–319.
[84] S. Mourdikoudis, R. M. Pallares, N. T. K. Thanh, *Nanoscale* **2018**, *10*, 12871–12934.
[85] W. Zhou, H. F. Greer, *Eur. J. Inorg. Chem.* **2016**, *2016*, 941–950.
[86] L. A. Giannuzzi, *Microsc. Microanal.* **2018**, *24*, 768–768.
[87] U. Holzwarth, N. Gibson, *Nat. Nanotechnol.* **2011**, *6*, 534–534.
[88] Peter. R. Griffiths, James. A. De Haseth, *Fourier Transform Infrared Spectrometry, 2nd Edition*, Wiley, **2007**.

Manuscript received: October 30, 2023